Computational and experimental investigations of an omni-flow wind turbine

P. Ying, Y.K. Chen[*], Y. Xu, and Y. Tian

School of Engineering and Technology, University of Hertfordshire, Hatfield, Herts, AL10 9AB, UK.

[*]Corresponding author, email: y.k.chen@herts.ac.uk

Abstract - Both numerical and experimental studies were conducted to evaluate the performance of an omni-flow wind turbine designed to provide renewable electricity on the top of urban buildings like skyscrapers. The numerical approach was based on Finite Volume Method (FVM) and the turbulence flow was studied with several commonly used Reynolds-averaged Navier-Stokes turbulence models. The results of the study were evaluated with the wind tunnel test results over a range of tip speed ratios. The numerical results showed the effect of blade number on both power output and starting capability. Although both the power and torque coefficient were improved significantly by the optimisation of the blade number, there was only a slight change when the blade number was greater than twenty. The results from wind tunnel testing also showed excellent starting capability with a starting wind velocity as low as 1.6 m/s. A numerical simulation was also conducted for the wind turbine working under non-uniform flow conditions. The numerical results have shown that the peak power coefficient of such a wind turbine under non-uniform flow, was lower than that under the uniform flow. Additionally, the applied thrust on a blade was subject to frequent and periodical changes. However, the effect of the change of thrust in magnitude and frequency was not significant. Therefore the omni-flow wind turbine has the potential to meet the challenge of unpredictable wind velocity and direction as a consequence of the urban environment.

Keywords: wind turbine; impulse turbine; omni-flow wind energy system; CFD; wind tunnel test; non-uniform flow

Nomenclature

c	chord of a blade aerofoil (m)	$U_{measure}$	measured flow velocity in the wind tunnel (m/s)
C_N	thrust coefficient		
C_P	power coefficient	$U_{uncovered}$	flow velocity in the entrance area for a uncovered model (m/s)
C_T	torque coefficient		
D	diameter of the chamber (m)		
F_D	drag (N)	v	component of $\vec{u}$ in y direction (m/s)
F_L	lift (N)		
F_N	thrust (N)	V_r	tangential velocity of a blade at r (m/s)
F_T	tangential force (N)		
L	length of the chamber (m)	w	component of $\vec{u}$ in z direction (m/s)
N	number of blades		
p	pressure (N/m^2)	W	relative wind velocity (m/s)
P	power output (W)	y^+	dimensionless wall distance
r	radius of a blade element (m)	λ	tip speed ratio

R	blade radius (m)	μ	dynamic viscosity of the fluid
S_M	momentum source term		$(N{\cdot}s/m^2)$
t	time (s)	ρ	fluid density (kg/m^3)
T	torque (Nm)	φ	angle between W and the
u	component of $\vec{u}$ in x direction		axis (°)
	(m/s)	ω	angular speed of the rotor
$\vec{u}$	velocity vector (m/s)		(rad/s)
U_∞	free stream wind velocity (m/s)	ABS	acrylonitrile butadiene styrene
U_1	velocity of the flow after	CFD	computational fluid dynamics
	passing guide vanes (m/s)	FVM	finite volume method
$U_{correct}$	corrected flow velocity in the	HAWT	horizontal axis wind turbine
	wind tunnel (m/s)	MRF	moving reference frame
$U_{covered}$	flow velocity in the entrance	SST	shear stress transport
	area for a covered model (m/s)	VAWT	vertical axis wind turbine

1. Introduction

Due to concerns on global warming and depletion of fossil fuels, renewable energy resources, especially wind energy, are receiving increasing attention in both academia and industries. A wind turbine is the energy conversion device to capture wind energy and translate that energy into electrical power. Large scale wind turbines are those with a rotor diameter larger than 5m [1]. Most modern large wind turbines are horizontal axis wind turbines (HAWTs) with two to three blades. Small wind turbines have been popular recently due to opportunities for local off-grid applications. Compared to large wind turbines that are employed for grid mainstream power generation, small wind turbines that function as distributed electricity generators can reduce the power losses in electricity transmission over long distances.

In the U.K., approximately 50% of energy consumption is in the building sector [2]. The UK Government has set a target of 80% carbon reduction by 2050 against a 1990 baseline [3]. The wind turbine integrated building is one of the emerging technologies that could provide substantial renewable energy and reduce CO_2 emission [4, 5]. There is an abundance of wind energy at the top of tall buildings for exploitation [6, 7]. Small wind turbines could be made suitable to be constructed on the top of buildings and provide electricity. However, conventional wind turbines have not been widely employed in an urban environment because of the limitation of existing wind turbine technologies and complex wind conditions in urban areas. Typically, due to low wind velocities in an urban area, a wind turbine requires a good starting capability [8]. A working noise is also one of key issues that wind turbines have not yet found a wide application in urban areas [9].

A novel omni-flow wind energy system was proposed for urban areas [10]. The aerodynamic characteristics of such a wind energy system was studied by Zhang [11] who performed computational fluid dynamics (CFD) analyses and experiments. Fig. 1 shows the 3-D model of this system. The system consists of five chambers, which are located along the

circumference of the shroud and form a vertical passage for entrainment of flow of the incoming wind. The omni-flow wind energy system was designed to better receive approaching wind from all directions, and to effectively transmit the wind to the air turbine located downstream. With this feature, the omni-flow wind energy system can cater for a wide variety of varying wind conditions. The velocities of the approaching wind can also be significantly accelerated due to the contraction of the nozzle structure. However, since the air flow only passes through one or two of the five chambers at any given time, as shown in Fig.1(b), the flow velocity distribution in front of the turbine is not uniform. The blades are under different flow velocities and as a consequence, undergo different aerodynamic loads during one operation cycle. Therefore it is difficult for a wind turbine with conventional thin blades to accommodate the flow conditions in the omni-flow wind energy system. It appears that the researches about a wind turbine have been focused on uniform flows [1, 12] although a wind turbine under a non-uniform flow condition has yet to be studied.
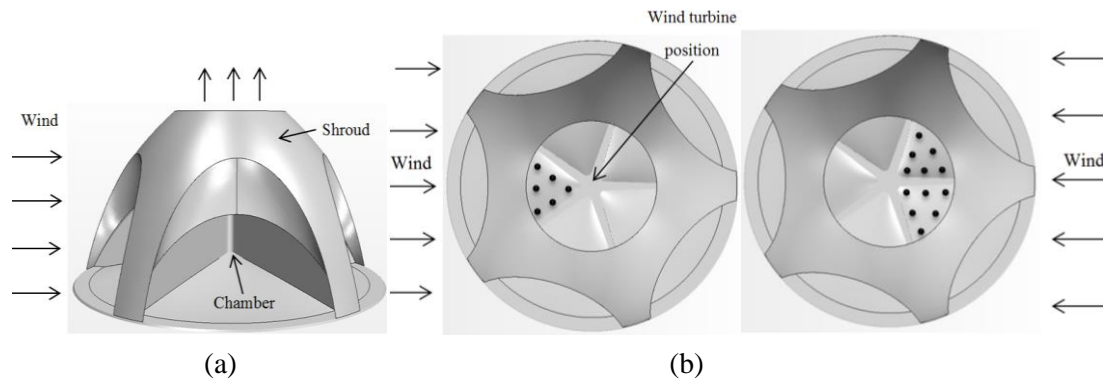

Fig. 1. A typical shroud of the omni-flow wind energy system: (a) schematic; (b) under different entrance flow of wind.

In recent papers [13, 14], it has been suggested that an impulse turbine has the potential to operate well under the variable air flow velocities in the marine environment. In the research field of wave energy, the impulse turbine has proven to be the best type of air turbine for both power generation and starting capability [15]. Considering these features, the impulse turbine principles appear attractive to the omni-flow wind energy system. However, there is little information on whether impulse turbine principles could be applied to a wind turbine.

The aim of this paper is to numerically investigate the aerodynamic features of a novel wind turbine based on impulse turbine principles. Under the conditions of both uniform and non-uniform flow, the numerical approach that was validated with wind tunnel experiments, has been used to study the power coefficient and torque coefficient. Additionally, other aerodynamic parameters of the wind turbine have been included in the study. Moreover the effect of blade number on the power coefficient and torque coefficient was also investigated. It is evident that this new wind turbine proposed in this paper has the potential to meet the requirements working with low noise and good starting capability in urban areas.

2. The wind turbine model

As shown in Fig. 2, the wind turbine consists of two components: a stator with guide vanes and a rotor with blades. Wind flow approaches the stator first and then leads to the rotor with the guide vanes. The omni-flow wind turbine is designed to work at the exit chamber of the shroud. Guide vanes are fixed to the surrounding wall of the exit chamber. As shown in Fig. 2(b), the guide vanes have thin plate geometry. The front part of a guide vane takes the shape of an arc and the rear part is straight. The straight part has a setting angle of 20°. Due to the geometric feature of the guide vanes, the flow velocity of the approaching wind will be accelerated. Meanwhile, the flow direction is also changed as a function of the setting angle of the rear part of the vane.
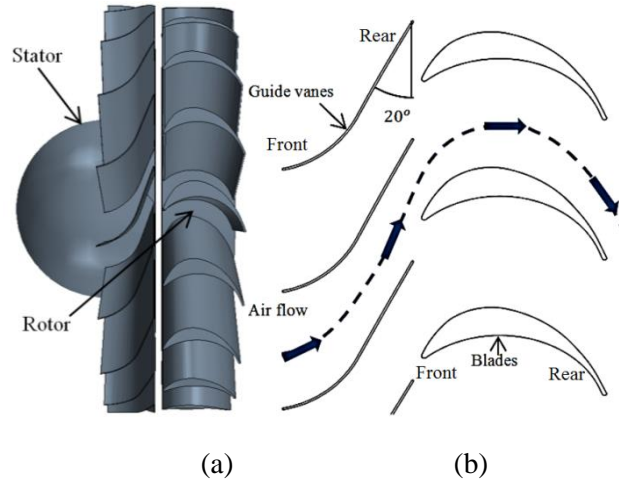

(a)   (b)

Fig. 2. A Schematic view of the wind turbine: (a) 3D view of the turbine model; (b) schematic view of guide vanes and blades.

The blades on the rotor used an aerofoil of the type found in a unidirectional impulse turbine. The rationale for using this type of blade aerofoil, was that it has the best power performance compared with other blade aerofoils in wave energy [16]. Based upon the sketch from Maeda et al [17], a further change of the blade aerofoil has been incorporated. Compared with conventional HAWTs, the omni-flow wind turbine employs a larger hub-to-tip ratio, which is defined as the hub diameter over blade diameter. The amount of the maximum aerofoil camber takes a 36% of the chord which is also larger than 0-6% of commonly used NACA aerofoils [18].

3. Aerodynamic analysis of the wind turbine

The omni-flow wind turbine was analysed by the blade element method, which is commonly used for the calculation of aerodynamic loads on blades and the power output of a wind turbine [19, 20]. This method refers to an analysis of forces at a section of the blade. For this wind turbine, the wind velocity diagram is shown in Fig. 3(a). U is the free-stream wind velocity, U_1 is the velocity of the flow after passing guide vanes, V_r represents the tangential

4

velocity of a blade at the radius r of an element and W is the relative wind velocity. The relationship between these velocities is shown below:

$$\vec{W} = \vec{U_1} + \vec{V_r} \tag{1}$$

The relative wind velocity is lower than the velocity of the flow after passing guide vanes. Force diagram of the blade aerofoil is shown in Fig. 3(b).
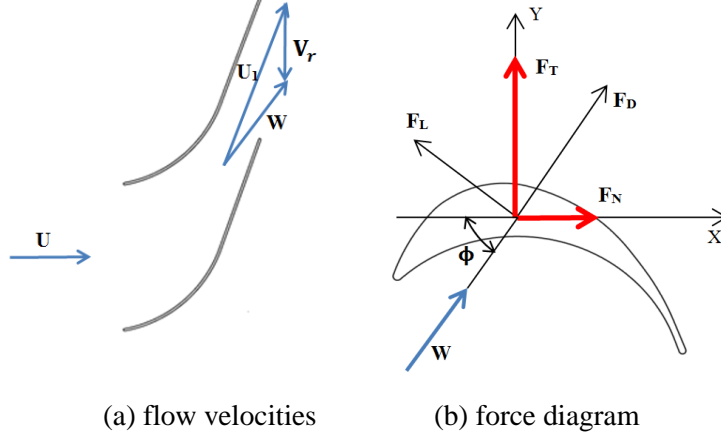

(a) flow velocities   (b) force diagram

Fig. 3. Velocities and forces on a blade element.

The tangential force F_T on the blade element can be expressed as

$$dF_T = dF_L \cos\phi + dF_D \sin\phi \tag{2}$$

and the axial force, F_N can be given by,

$$dF_N = -dF_L \sin\phi + dF_D \cos\phi \tag{3}$$

where F_L and F_D represent lift and drag respectively, and ϕ is the angle between the relative velocity and the rotating axis. It should be noted that both lift and drag forces contribute to the tangential force in this case as such wind turbine is driven by dual forces: lift and drag.

The torque T on an element can be calculated as follows:

$$dT = Nr\left(dF_L \cos\phi + dF_D \sin\phi\right) \tag{4}$$

where N denotes the total number of blades.

The power output P on an element can then be expressed as

$$dP = \omega dT \tag{5}$$

where ω is the angular speed of the rotor.

4. Experimental apparatus

Experimental studies were carried out in a closed return wind tunnel at the University of Hertfordshire. The tunnel had a test section of 1.14m (width) × 0.84m (height), with a maximum wind velocity of 25 m/s. The flow uniformity was greater than 99% and the turbulence intensity was less than 1%. As shown in Fig. 4, a wind turbine test rig was located

5

at the centre of the test section. The stator and rotor were produced by rapid prototyping technology with acrylonitrile butadiene styrene (ABS) plastic wires. The turbine had 20 guide vanes with a diameter of 300 mm and 20 blades with a diameter of 296 mm. The hub diameter of this turbine was 135 mm. Both stator and rotor had an identical hub diameter. The wind turbine was installed inside a 200 mm long cylindrical chamber. The guide vanes were fixed to the chamber wall. There was a clearance of 2 mm between the blade tip and chamber wall. The gap between the blade tip and chamber wall was to accommodate the safe installation of the rotor within the chamber. The 2 mm clearance was approximately 1% of the rotor radius. It is accepted practice that a clearance of 1% has a negligible influence on the performance of an impulse turbine [21].

Fig. 4 also shows the test rig and its primary measurement system that was utilised in this study. The torque applied on the turbine shaft was measured by a torque transducer (Datum M420), which had a test range from 0 Nm to 10 Nm (measurement accuracy within 0.1%). Rotational speeds of the wind turbine were also obtained from the torque transducer and the maximum rotational speed of the transducer was 5000 rpm. A pair of spur gears was used to transmit the torque from the shaft of the wind turbine to the shaft of the torque transducer. The shaft of the turbine was supported by house bearings. A DC motor was connected to the torque transducer to generate a load, which was adjusted by changing the current in the motor.
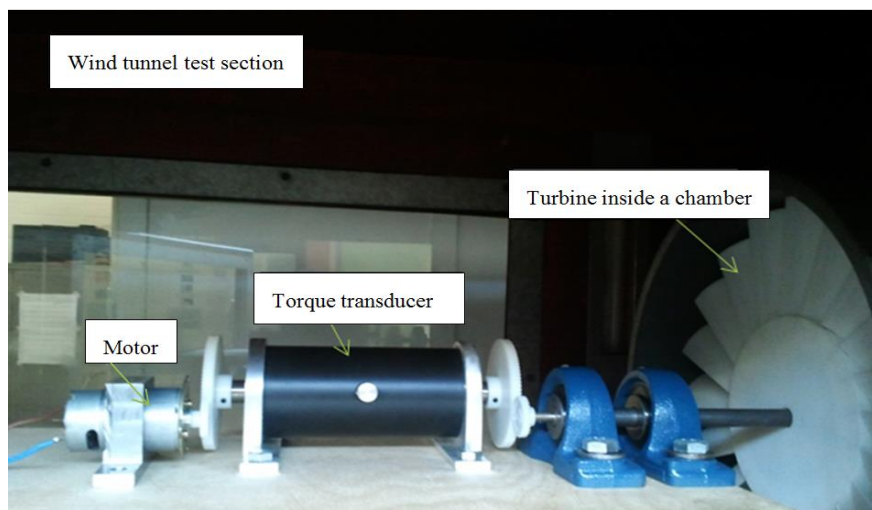

Fig. 4. Test rig within the wind tunnel test section.

The power loss through the bearings and gears in experiments has been considered. An average value of the error in power output was about 1% caused by bearings and 1.6% by gears. Hence, the total error can be calculated as

$$\text{Total error} = \sqrt{1\%^2 + 1.6\%^2} = 1.9\% \tag{6}$$

Since this wind turbine was tested in a closed test section, the blockage effect was considered by a suggested approach [22] and the correction factor is about 0.03 for the flow velocity inside the tunnel. Therefore, flow speed inside the test section can be expressed as

$$U_{correct} = 1.03 \ U_{measure} \tag{7}$$

5. Numerical principles and computational techniques

The present computational study was conducted using Finite Volume Method (FVM). The air flow was assumed to be incompressible. The governing equations consisted of the continuity equation and momentum equation [23]:

Continuity equation

$$\frac{\partial \rho}{\partial t} + \text{div}(\rho \vec{u}) = 0 \tag{8}$$

where ρ denotes the fluid density, t is time and $\vec{u}$ denotes the velocity vector.

Momentum equations

x-momentum $\qquad \dfrac{\partial(\rho u)}{\partial t} + \text{div}(\rho u \vec{u}) = -\dfrac{\partial p}{\partial x} + \text{div}(\mu \ \text{grad} \ u) + S_{Mx}$ $\tag{9a}$

y-momentum $\qquad \dfrac{\partial(\rho v)}{\partial t} + \text{div}(\rho v \vec{u}) = -\dfrac{\partial p}{\partial y} + \text{div}(\mu \ \text{grad} \ v) + S_{My}$ $\tag{9b}$

z-momentum $\qquad \dfrac{\partial(\rho w)}{\partial t} + \text{div}(\rho w \vec{u}) = -\dfrac{\partial p}{\partial z} + \text{div}(\mu \ \text{grad} \ w) + S_{Mz}$ $\tag{9c}$

where u, v and w are the components of the velocity vector $\vec{u}$ in x, y and z directions, respectively, μ is the dynamic viscosity of the fluid, p is the pressure, and S_M is the momentum source term to account for the viscous stress.

Due to computational resources, four two-equation turbulence models based on the Reynolds-averaged Navier-Stokes equations were considered to choose. The standard k-ε turbulence model is the most widely used two-equation turbulence model due to its reasonable accuracy for a variety of applications. However, this turbulence model has a poor performance in some important cases such as rotating flows [23]. Realizable k-ε model is an advanced k-ε model [24]. It is possible to produce a better performance for the flows involving rotation, separation and recirculation. The realizable k-ε model is one of the most successful recent developments in the k-ε model family [25]. Standard and realizable k-ε models can utilise a two-layer treatment in the near-wall region to reduce grid dependence and to improve numerical stability [23]. Apart from the family of k-ε models, the standard k-ω model is another prominent two-equation turbulence model. The standard k-ω model does not require wall-damping functions in low Reynolds number applications [23, 26]. The near-wall performance of the standard k-ε model is unsatisfactory for boundary layers with adverse pressure gradients, hence a Shear Stress Transport (SST) k-ω model developed from k-

7

ω model, was proposed [23, 27]. The SST k-ω model can provide more accurate and reliable results than the standard k-ω model in a wide range of applications [28]. Four turbulence models, standard k-ε, realizable k-ε, standard k-ω and SST k-ω models, all have been employed for wind turbines and impulse turbines [5, 28-30]. In order to assess the best numerical configuration, the performance of four turbulence models would be validated with wind tunnel tests.
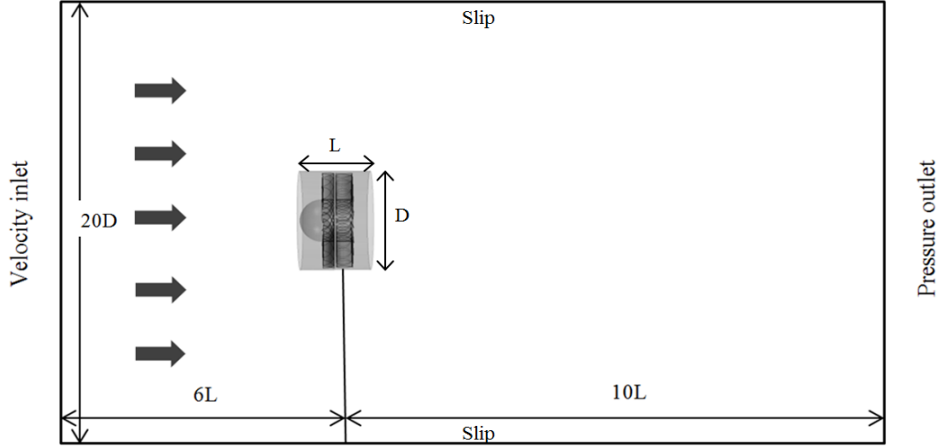

Fig. 5. Schematic view of the computational domain setup in simulations.

To investigate performances of the omni-flow wind turbine, a three-dimensional analysis was carried out through the software package: Star-CCM+. The computational domain with the wind turbine model is shown in Fig.5. The domain was 16 times the length (L) of the chamber in the axial direction, and both the domain width and height were 20 times the rotor diameter (D) of the wind turbine. Such a large domain will ensure that the blockage effect of walls does not influence the flow around the wind turbine [31]. The upstream boundary condition was set as the velocity inlet and downstream boundary condition was set as the pressure outlet, as shown in Fig. 5. Surrounding walls of the domain were specified as slip and surfaces of the wind turbine were no-slip. Moving Reference Frame (MRF) was chosen for modelling rotational effects in this work. MRF used in investigations of wind turbines and impulse turbines has showed accurate results validated by experiments [32, 33]. Sliding mesh technology has not been employed in this study because it needs more computing power for such complex 3-D geometry. Steady state was combined with the MRF in simulations. Rotational speeds were simulated from 0 rpm to 600 rpm for a free entrance stream velocity of 8.2 m/s. The value of tip speed ratio (λ) was varied by assigning different values of angular velocity as below:

$$\lambda = \omega R/U \tag{10}$$

The convergence to the final steady-state was assessed with a maximum amount of 2000 iterations, which was always sufficient to reach the final computed residual of 10^{-4}.

Due to the complex geometry, unstructured polyhedral cells were suitable and employed in meshing [25]. In order to obtain the dimensionless wall distance $y^+ < 5$, the distance of the first grid layer from the blade was 0.15 mm and total 8 layers were generated with a growth rate of 1.5 [23, 32]. Fig. 6 shows the section view of the meshed model. A mesh independency test was conducted with a cell number ranging from 3,300,000 to more than 7,000,000. As shown in Fig. 7, when the cell number exceeded 6,000,000, the resulting difference between fine cells and coarse cells was less than 0.1%. Therefore, all cases in this study had around 6,000,000 polyhedral cells.
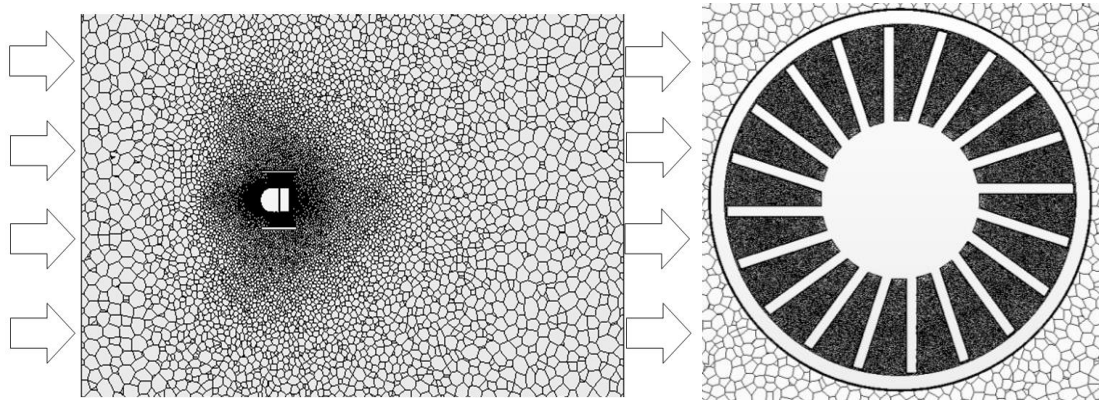

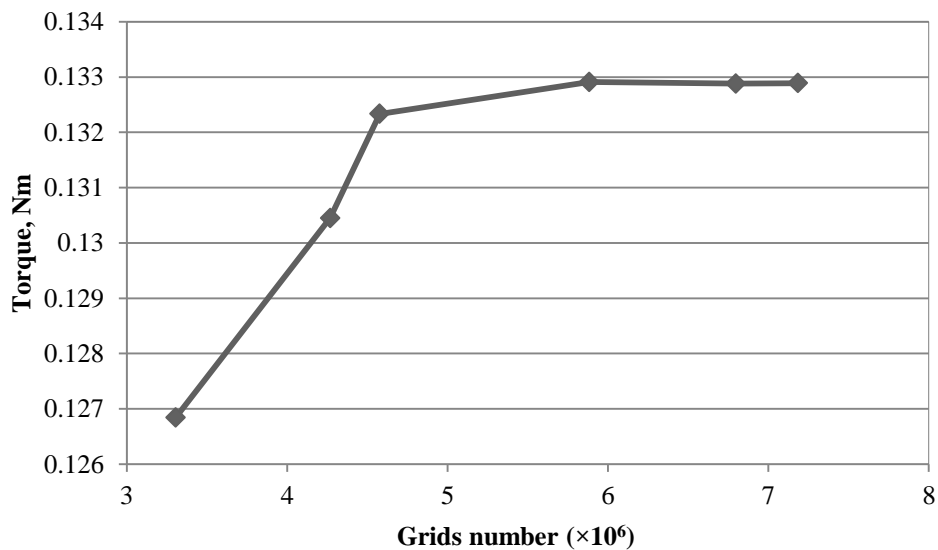**Fig. 6.** Two section views of the meshed model.

Fig. 7. Torque values under different grid numbers.

As shown in Fig. 1(b), only one or two of the five chambers in this novel omni-flow wind energy system can take the entrance wind flow at any given time. This resulted in the non-uniform flow inside the chambers in front of the turbine. Passing flow occupies about 20%

to 40% of the entrance area and negligible wind flowed existed in the remaining regions. In order to simulate the non-uniform flow condition, a cover was added in the front of the wind turbine model as shown in Fig. 8(a). The cover created the restrained flow, which occupied the original entrance area by a percentage of 20% to 40%.
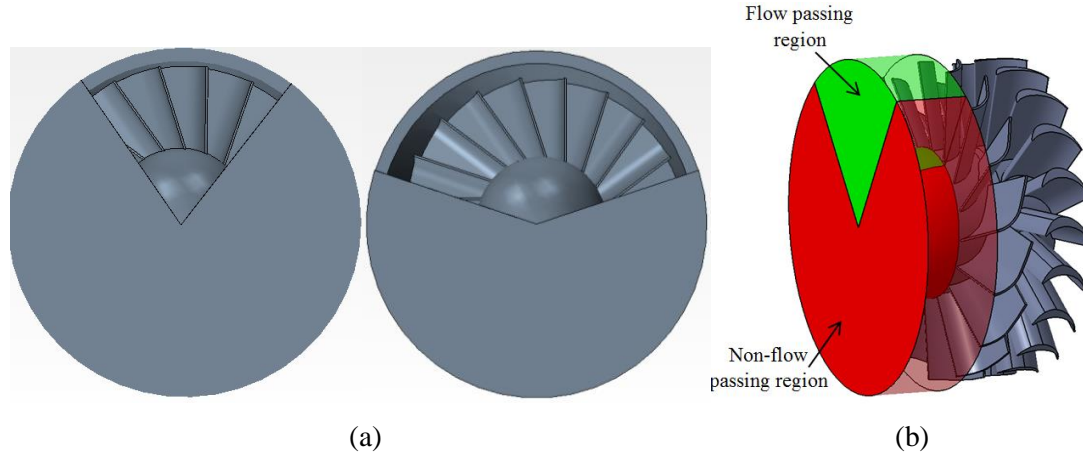

Fig. 8. Wind turbine models in simulations: (a) models with 20% and 40% entrance area; (b) two flow regions ahead the turbine.

There were two main features in the models shown in Fig. 8. The first feature enables the approaching flow near the turbine to be divided into flow passing region and non-flow passing region as shown in Fig. 8(b). The flow properties in the two separate regions were different, but had an influenced on each other. The aerodynamic behaviour of the flow on the blades in both regions was simulated in parallel. The second feature, whereby the partial flow was blocked in the axial direction by the cover, generated a high pressure at the front of the cover, and accelerated flow speeds in the entrance area. Therefore, a correction was needed to consider the cover effect on flow velocities. A factor for the correction is defined as the ratio of the averaged flow velocities of the approaching flow between when it is covered and uncovered: $U_{covered}$ / $U_{uncovered}$. $U_{covered}$ represents an averaged flow velocity in the entrance area. $U_{uncovered}$ is the averaged flow velocity for the model without the cover in the same testing area as $U_{covered}$. This ratio represents the value change of approaching flow velocity due to the cover effect. The averaged velocity $U_{covered}$ and $U_{uncovered}$ were obtained from CFD simulations. The correction factor was 1.56 for an entrance area of 20% and 1.2 for an entrance area of 40%, respectively. Therefore the corrected flow velocity was 12.8 m/s for the model with 20% entrance area and 9.8 m/s for the model of 40% entrance area in an oncoming flow velocity of 8.2 m/s.

6. Results and discussion

Three-dimensional steady, turbulent incompressible simulations with the MRF to represent the rotor motion were carried out. Aerodynamic features of this wind turbine model

were analysed in a range of tip speed ratios. The power coefficient, torque coefficient and thrust coefficient were presented quantitatively to illustrate the performance of this wind turbine under different conditions.

The power coefficient (C_P) can estimate the capability of power generation for a wind turbine and is defined as the ratio of the shaft power (P) from a wind turbine to the power available from wind [18]:

$$C_P = P/(0.5\rho U^3 \pi R^2) \tag{11}$$

Torque coefficient (C_T) is used to assess the mechanical torque generated by the wind turbine. Wind turbines with higher value of C_T can start and work at lower wind velocity [34]. Torque coefficient is defined as [35]:

$$C_T = C_P/\lambda = T/(0.5\rho U^2 \pi R^3) \tag{12}$$

Apart from the tangential force, there is an axial force or thrust F_N acting on a blade, as shown in Fig. 3(b). A dimensionless term, thrust coefficient, can be used to estimate the thrust of a wind turbine [20], shown below:

$$C_N = F_N/(0.5\rho U^2 \pi R^2) \tag{13}$$

6.1. Comparison of numerical results with the wind tunnel test results

Fig. 9 shows the experimental results of this wind turbine under different flow velocities within the wind tunnel. It can be seen that at a given flow velocity of 8.2 m/s the output torque varies with the rotational speed of the turbine. With an increase of the rotational speed the torque decreased gradually and the maximum torque is about 0.28 Nm. The maximum torque occurred when the wind turbine was stationary. As shown in Fig. 9, the errors of measurement were about 1.9%.
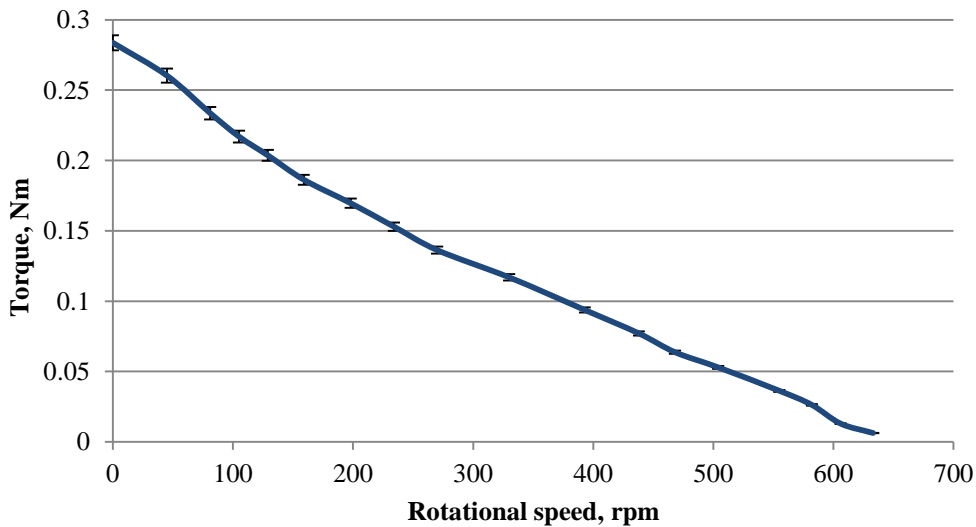

Fig. 9. Output torque verse rotational speed under a wind velocity of 8.2 m/s.

The numerical simulations were conducted with several turbulence models and the simulation results were compared with experimental data to validate the numerical approach. Four turbulence models, standard k-ε, realizable k-ε, standard k-ω and SST k-ω turbulence models, were evaluated for the wind turbine model with 20 blades and under the condition of uniform flow. The wind turbine model in simulations had the same dimension as the experimental prototype. Based upon the values of torques shown in Fig. 9, an experimental power coefficient was calculated by Eqs. (5) and (11) and presented in Fig. 10.
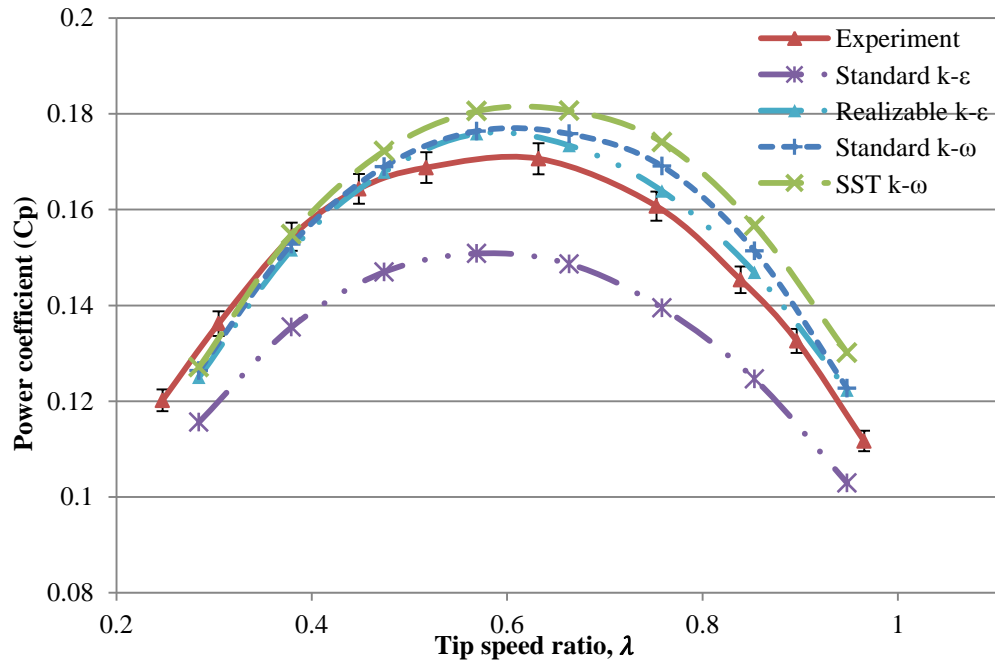

Fig. 10. Power coefficient comparison with experimental data at different tip speed ratios .

Fig. 10 shows the comparison of power coefficients between the results from numerical simulation and experimental results under a flow velocity of 8.2 m/s. It can be seen that the numerical simulation results from all four turbulence models had a similar trend of power coefficient versus tip speed ratio to that from the experimental results. Apart from the standard k-ε model, the numerical results from the other three models agree well with the experimental results. The standard k-ε turbulence model produced lower results compared with the experimental ones across the whole range of tip speed ratios. With the tip speed ratio exceeding 0.5, the power coefficient resulted from the SST k-ω model is about 6% higher than the experimental one. Maximum power coefficients from both the realizable k-ε model and the standard k-ω model correlated well with the maximum power coefficient from the experiment. It is suggested that the numerical approach with realizable k-ε model can provide reliable results and thus was employed for the rest of this study. The results in Fig. 10 also show that the $C_p - \lambda$ curve was nearly symmetric at the tip speed ratio of 0.6 and the maximum C_p was obtained at this tip speed ratio.

6.2. Blade number effect on power output and starting capability

Fig. 11 shows the distribution of power coefficients versus tip speed ratio under 5 different blade numbers of 15, 17, 20, 25, and 30. It can be seen that at the low values of tip speed ratios, differences caused by various blade numbers were small. Near the middle value (0.6) of tip speed ratio all models reached their maximum value of C_P. The maximum power coefficient had two increments of about 10% with the blade number increasing from 15 to 17 and 17 to 20. Furthermore, no significant improvement of the maximum power coefficient was found when the blade number was over 20. It is suggested that the blades contributed to the blocking of passing flow to a certain degree, when the turbine had more than 20 blades. As shown in Fig. 11, the range of tip speed ratio values was from 0.1 to 1.2 which was smaller than that of HAWT. These low tip speed ratios are dependent upon the velocity relationship as shown in Fig. 3(a). The small range of tip speed ratios means that the omni-flow wind turbine works at low rotational speeds and as a result, with a low level of noise [9]. Irrespective of the number of blades the tip speed ratio was approximately 0.6 which yielded the highest power coefficient for each blade number.
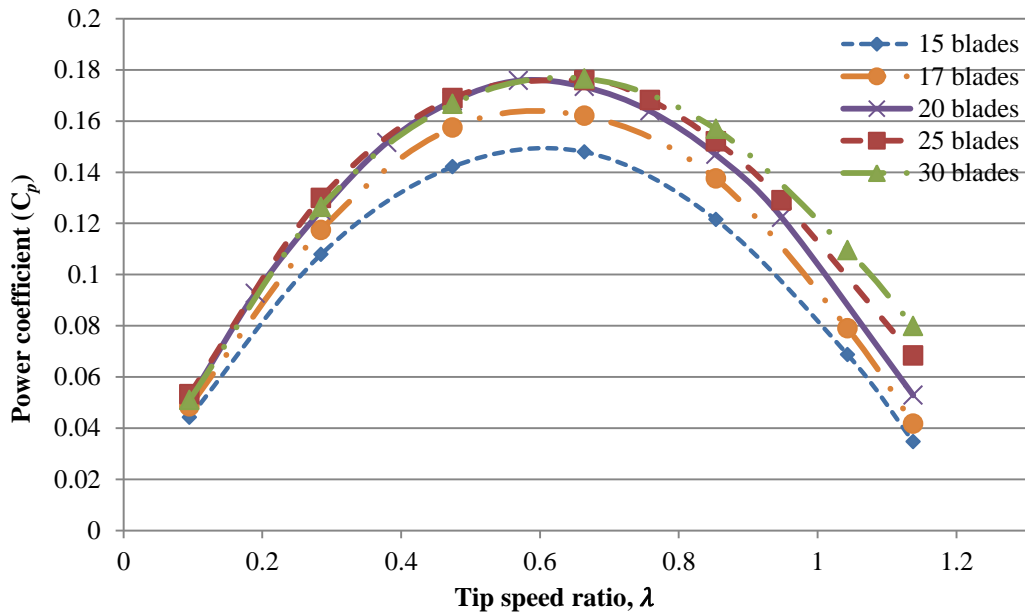

Fig. 11. Power coefficient versus tip speed ratio for various blade numbers.

Fig. 12 shows the relationship between torque coefficients and tip speed ratios. It can be seen that the $C_T - \lambda$ curves were nearly linear. When the wind turbine was stationary, the maximum C_T was in the range from 0.5 to 0.6 with various blade numbers. Then C_T decreased to zero gradually with tip speed ratios increasing. No significant difference was found in the torque coefficient of this turbine with more than 17 blades. It is also noted that the maximum C_T of such wind turbine was much greater than that of other wind turbines [35]. For a general

HAWT the maximum C_T is lower than 0.1. It is possible to conclude that this turbine has good starting capability.
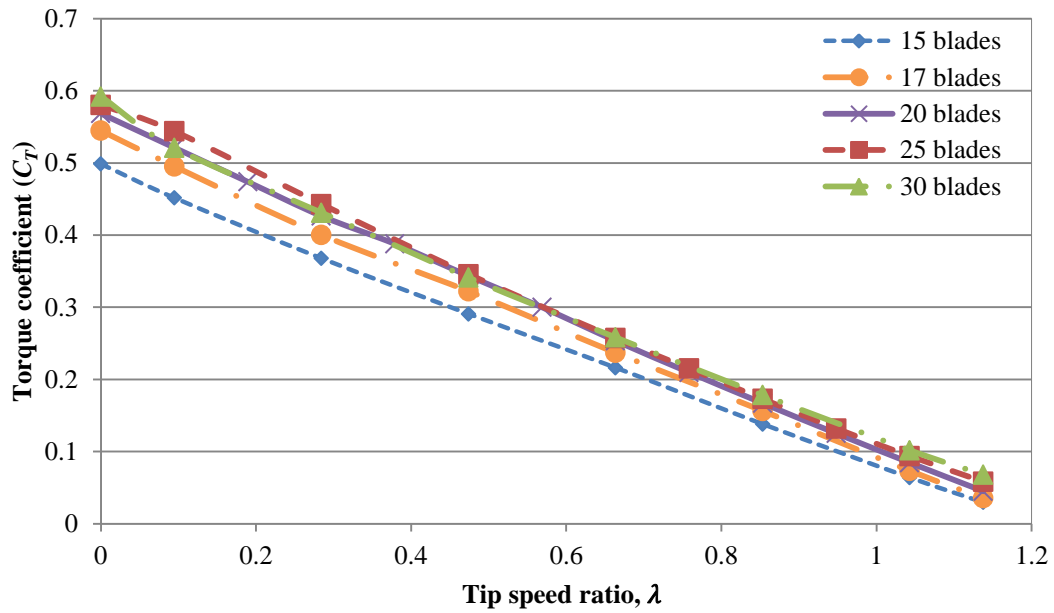

Fig. 12. Torque coefficient versus tip speed ratio for various blade numbers.
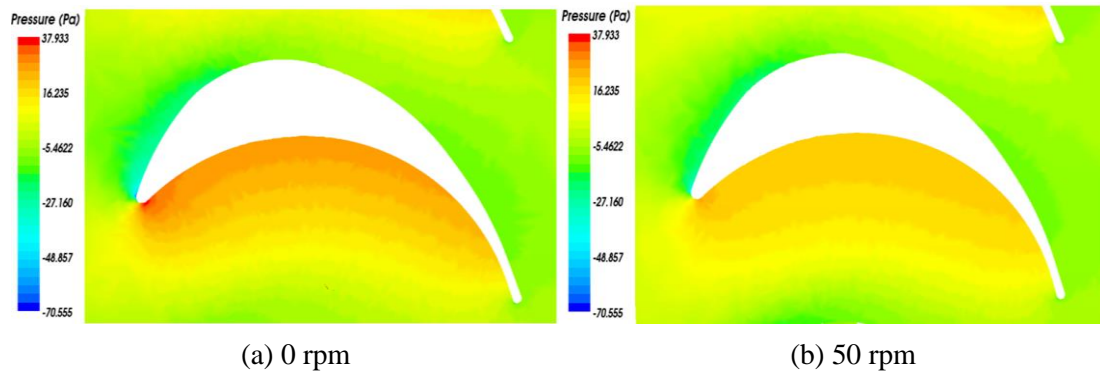

(a) 0 rpm   (b) 50 rpm

Fig. 13. Pressure distribution around a blade.

Fig. 13 shows the pressure distribution on the periphery of the blade at a radius of 0.13 m under rotational speeds of 0 rpm and 50 rpm. It was found that a large pressure difference region occurred at the leading edge which produced the high value of the starting torque. At blade starting, the magnitude of the pressure difference decreased, and the torque generated was reduced.

To validate the starting capability of this novel wind turbine, a series of wind tunnel tests were performed on a 20 blade wind turbine. Fig. 14 shows the relationship between maximum rotational speeds and starting wind velocities. Tests were carried out on an unloaded wind turbine. As starting wind velocity increases, the maximum rotational speed of the wind turbine correspondingly increases. In particular, it can be seen that the wind turbine can start

to rotate with a rotation speed of 15 rpm at the lowest wind velocity of 1.6 m/s, demonstrating the excellent starting capability of this novel device. It is well known that the available wind blowing in urban areas has low wind velocity. It is reported that in Great London urban area, only 27 % of that area has a wind velocity exceeding 4 m/s [8]. It is possible to conclude that in urban areas, the omni-flow wind turbine with the advantage of an excellent starting capability can capture wind energy with low wind velocities.
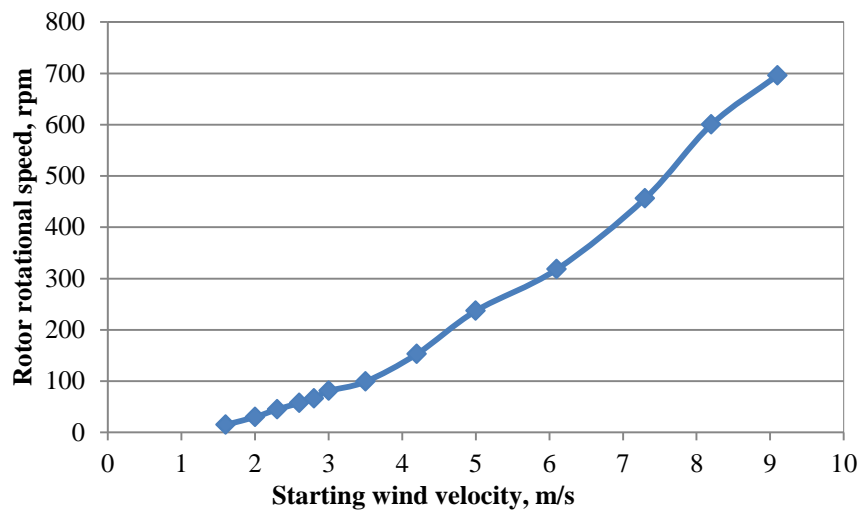

Fig. 14. Experimental maximum rational speeds versus starting wind velocities.

The thrust coefficient distribution of this wind turbine with different blade numbers versus the tip speed ratio is shown in Fig. 15. It can be seen that the thrust coefficient increases with tip speed ratios and blade numbers. The maximum thrust coefficient of this wind turbine was approximately 0.3, which was much smaller than about 1 of a HAWT [18]. Solidity is defined as the total blade area divided by the blade swept area [20]. It is accepted knowledge, that the larger the solidity of a wind turbine, a higher thrust coefficient is produced [18]. Calculations have shown that the turbine model with 25 blades or 30 blades had a solidity of greater than 1. By comparison, a general 3 blades HAWT possesses a solidity of about 0.1[20]. However, as shown in Fig. 15, the high solidity of this wind turbine was not associated with a great thrust coefficient. This means that the bending moment applied to the blades from the thrust is much smaller than that of a conventional blade. It is suggested that the effect of thrust is small.
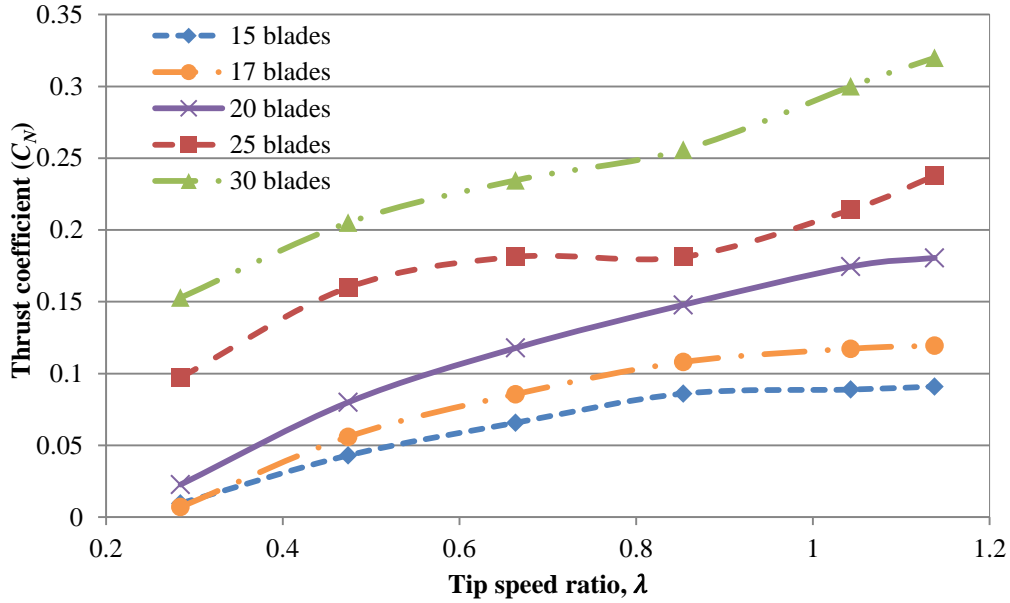
Fig. 15. Thrust coefficient versus tip speed ratio for various blade numbers.

Figs. 11-12 indicate that the blade number greatly influences the power generation and starting capability. By increasing the blade number, this wind turbine can produce more power and start to rotate at a lower wind speed. However, a turbine with more than 20 blades results in no significant change of power outputs and torques. Considering the cost of materials and manufacturing process, a rotor blade number of 20 is considered to be the optimum.

As discussed in this section, this new wind turbine has two unique features: low working noise and good starting capability, compared with conventional wind turbines. This suggests that this wind turbine has the potential to be employed in urban areas [36]. This new wind turbine can be integrated with the omni-flow wind energy system as shown in Fig. 1 and is suitable to be installed on the tops of buildings [10, 11, 37]. Compared with some wind turbines [38], this wind turbine can be driven by omni wind flows with an aid of the omni-flow wind energy system. Moreover, the turbine works inside a shroud of the system, which can contain a possible damage from a blade fail-off.

6.3 Effect of non-uniform flow on the aerodynamic behaviour of the turbine

When the entrance flow was non-uniform, the blades of this wind turbine experienced different aerodynamic effects. The power coefficient and torque coefficient of this wind turbine with 20 blades under the non-uniform flow condition are shown in Fig. 16. Both C_P and C_T were obtained when 20% and 40% of flow entrance area and corrected flow velocities were applied to Eqs. (11) and (12).

16

It appears that this wind turbine with non-uniform flow has a range of peak power coefficients from 0.06 to 0.12, which is reduced by 29% - 65% compared with maximum C_P shown in Fig. 11. And the range of tip speed ratios decreased to less than 1. There was no change for the model with 40% entrance area on the maximum C_T. However, it is noted that the omni-flow wind energy system could result in accelerating the approaching flow and then guided flow through the wind turbine. Therefore, if whole system is considered, a system that couples an omni-flow wind energy system and this wind turbine, then the combined result has the potential to produce a larger output power and an improved starting capability [37].
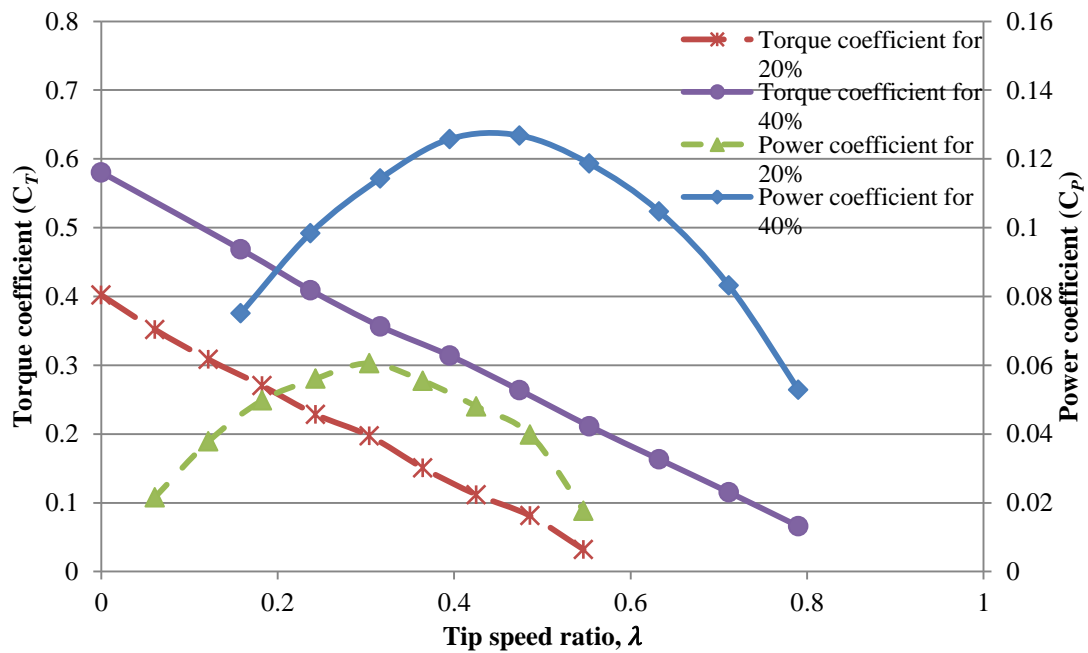

Fig. 16. Torque coefficient and power coefficient versus tip speed ratio with 20% entrance area and 40% entrance area.

Fig. 17 shows the torque on each blade under non-uniform flow. The main torque of this wind turbine was generated from the blades in the flow passing region. It can be seen that with the tip speed ratio increasing, the values of torque for every blade decreased. In the case of the model with 20% entrance area, the negative torque was generated on No. 10-20 blades which could affect the rotor rotating. For the model with 40 % entrance area, a negative torque was also produced on No. 14-20 blades. Compared with the positive torque, the values of negative torque are significantly small when the turbine is rotating with a low tip speed ratio. However, with a high tip speed ratio of 0.55, the negative torque in the model with 20 % entrance area was about 38% of overall generated torque. In this case the outcome resulted in a small range of tip speed ratios and low power coefficients as shown in Fig. 16. The negative torque also affected the power output in the model with 40% entrance area. As shown in Fig.8, only four blades in the model with 20 % flow entrance area were directly exposed to the flow due to the cover. However the simulation results as shown in Fig. 17 indicated that eight

blades had generated positive values of torques. From the study it has been shown that there was a transition zone of flow between flow passing region and non-flow passing region. Therefore, the transition zone resulted in more than four blades taking the flow and producing positive torque. It was observed in CFD simulations that the generation of transition zone was due to flow pressure difference between two regions.
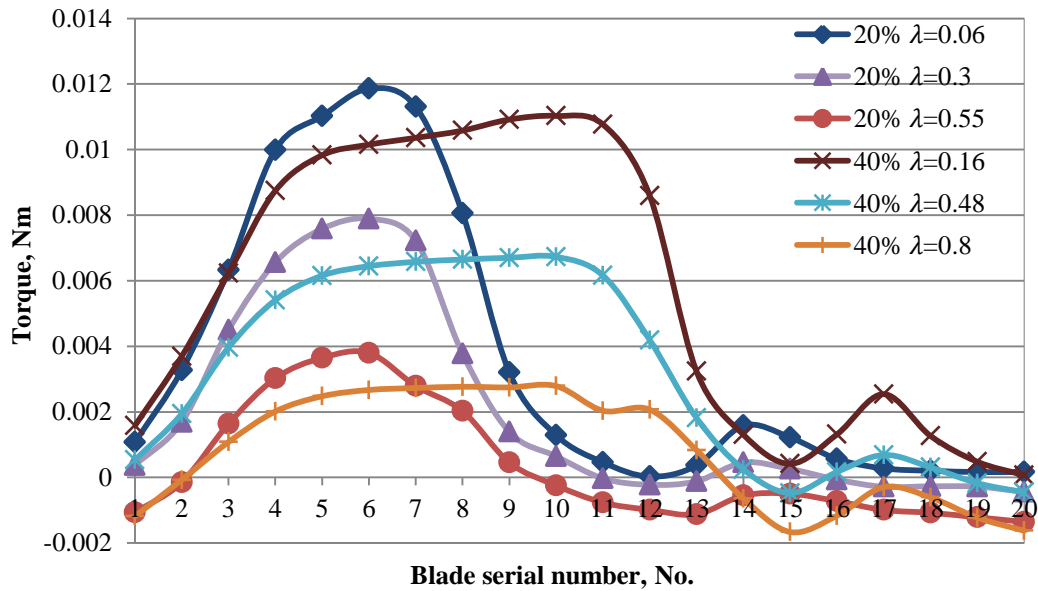

Fig. 17. Torque generated on every blade under 20% entrance area and 40% entrance area.
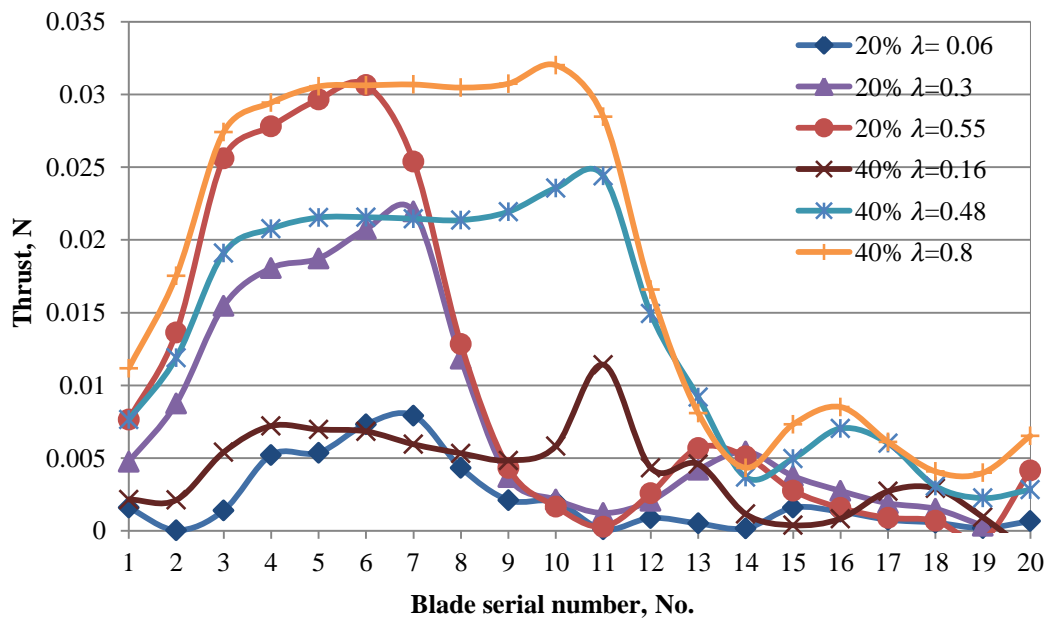

Fig. 18. Thrust on every blade under 20% entrance area and 40% entrance area.

The thrust on each blade under non-uniform flow is shown in Fig. 18. The blades in the flow passing region generated a larger thrust than in the non-flow passing region. The values

of the thrust increased with a larger tip speed ratio. The thrust force can generate a bending moment on a blade as shown in Fig. 3(b). Due to the small values of the thrust, the bending moments generated on the blades are also fairly small. The thrust on a blade is not constant during one operation cycle. It is noted that during one operation cycle, each blade experiences a significant change of thrust twice. For the wind turbine model with 40% entrance area, the rotational speed at the maximum C_P is around 300 rpm. It was calculated that the thrust change frequency was 10 Hz. For the wind turbine model with 20% entrance area, the thrust change frequency was about 8 Hz. Based upon the definition of tip speed ratios, the frequency of the thrust change would decrease with the increase of the rotor radius. When the wind turbine has a rotor radius of 1 m, the thrust change frequency would be decreased to 1.5 Hz. Due to the definition of the dimensionless thrust coefficient, the maximum thrust on a blade is about 1.4 N when the rotor radius is 1 m. It can be suggested that magnitude and change frequency of the thrust are marginal.

7.   Conclusions

An aerodynamic investigation of an omni-flow wind turbine designed for urban areas has been carried out with both numerical and experimental methodologies. Based upon the results and discussion, the following conclusions can be drawn:

1) Four turbulence models in CFD simulation have been studied. The simulation results of this novel wind turbine from the realizable k-ε turbulence model achieved a good correlation with the experimental data from wind tunnel tests.
2) The effect of the blade number on power coefficient was studied numerically with the realizable k-ε turbulence model. The values of power coefficients of this wind turbine were increased significantly with an increase of the blade number before the blade number reached 20. There was a slight improvement of power coefficient values when the blade number was greater than 20. It is evident that a blade number of 20 is the optimal choice for a more efficient power generation.
3) From the wind tunnel testing, this innovative omni-flow device had excellent self-starting capability. The omni-flow wind turbine demonstrated a starting capability for a wind velocity as low as 1.6 m/s. This feature enables the wind turbine to function with low wind velocities found in an urban area.
4) The performance of this wind turbine under non-uniform flow was investigated. The maximum power coefficient of this wind turbine with 20% - 40% non-uniform flow entrance area was 0.06 – 0.12 which was lower than that under uniform flow by 29% - 65%.

5) A study of load distribution of this wind turbine under non-uniform flow showed that the thrust applied on a blade changed through a rotational period. However, the influence of the thrust change in magnitude and frequency is marginal.

References

[1] Kishore RA, Coudron T, Priya S. Small-scale wind energy portable turbine (SWEPT). J Wind Eng Ind Aerodynam 2013;116:21-31.

[2] UK Department for Communities and Local Government. Improving the energy efficiency of our homes and buildings - energy certificates and air-conditioning inspections for buildings; 2008.

[3] UK Office of Public Sector Information. Climate Chang Act 2008; 2008.

[4] Peacock AD, Jenkins D, Ahadzi M, Berry A, Turan S. Micro wind turbines in the UK domestic sector. Energy Build 2008;40:1324-33.

[5] Chong WT, Fazlizan A, Poh SC, Pan KC, Hew WP, Hsiao FB. The design, simulation and testing of an urban vertical axis wind turbine with the omni-direction-guide-vane. Appl Energy 2013;112:601-9.

[6] Balduzzi F, Bianchini A, Carnevale EA, Ferrari L, Magnani S. Feasibility analysis of a Darrieus vertical-axis wind turbine installation in the rooftop of a building. Appl Energy 2012;97:921-9.

[7] Merten S. Wind Energy in the Built Environment. Brentwood, UK: Multi-Science; 2006.

[8] Drew DR, Barlow JF, Cockerill TT. Estimating the potential yield of small wind turbines in urban areas: a case study for Greater London, UK. J Wind Eng Ind Aerodynam 2013;115:104-11.

[9] Rogers AL, Manwell JF, Wright S. Wind Tubrine Acoustic Noise. Amherst, USA: Renewable Energy Research Laboratory, University of Massachusetts at Amherst; 2002.

[10] Sureshan V. Omni-directional wind power station. Patent no. WO2008017106A1; 2008.

[11] Zhang X, Chen YK, Calay R. Modelling and analysis of a novel wind turbine structure. Int J Model Ident Control 2013;19:142-9.

[12] Bontempo R, Manna M. Performance analysis of open and ducted wind turbines. Appl Energy 2014;136:405-16.

[13] Setoguchi T, Santhakumar S, Maeda H, Takao M, Kaneko K. A review of impulse turbines for wave energy conversion. Renew Energy 2001;23:261-92.

[14] Thakker A, Usmani Z, Dhanasekaran TS. Effects of turbine damping on performance of an impulse turbine for wave energy conversion under different sea conditions using numerical simulation techniques. Renew Energy 2004;29:2133-51.

[15] Setoguchi T, Takao M. Current status of self rectifying air turbines for wave energy conversion. Energ Convers Manage 2006;47:2382-96.

[16] Jayashankar V, Anand S, Geetha T, Santhakumar S, Jagadeesh KV, Ravindran M, et al. A twin unidirectional impulse turbine topology for OWC based wave energy plants. Renew Energy 2009;34:692-8.

[17] Maeda H, Takao M, Setoguchi T, Kaneko K, Kim TH, Inoue M. Impulse turbine for wave power conversion with air flow rectification system. In: Proceedings of the

Eleventh International Offshore and Polar Engineering Conference, Stavanger, Norway; 2001.

[18] Burton T, Sharpe D, Jenkins N, Bossanyi E. Wind energy handbook. Chichester, UK: John Wiley & Sons Ltd.; 2001.

[19] Aslam Bhutta MM, Hayat N, Farooq AU, Ali Z, Jamil SR, Hussain Z. Vertical axis wind turbine – a review of various configurations and design techniques. Renew Sustain Energy Rev 2012;16:1926-39.

[20] Manwell JF, McGowan JG, Rogers AL. Wind Energy Explained - theory, design and application. Chichester, UK: John Wiley & Sons Ltd.; 2002.

[21] Thakker A, Dhanasekaran TS. Computed effects of tip clearance on performance of impulse turbine for wave energy conversion. Renew Energy 2003;29:529-47.

[22] Barlow JB, Jr. Rae WH, Pope A. Low-speed Wind Tunnel Testing. Third ed. New York, US: John Wiley & Sons Ltd.; 1999.

[23] Versteeg HK, Malalasekera W. An introduction to computational fluid dynamics - the finite volume method. Second ed. Harlow, UK: Pearson Education Ltd.; 2007.

[24] Shih T, Liou WW, Shabbir A, Yang Z, Zhu J. A new k- eddy viscosity model for high reynolds number turbulent flows. Comput Fluids 1995;24:227-38.

[25] Star-ccm+ user guide 6.04. New York, US; CD-adapco; 2011.

[26] Wilcox DC. Turbulence modelling for CFD. La Canada, US: DCW Industries Inc.; 1993.

[27] Menter F. Two-equation eddy-viscosity turbulence model for engineering applications. AIAA Journal 1994;32:1598-605.

[28] Dragomirescu A. Performance assessment of a small wind turbine with crossflow runner by numerical simulations. Renew Energy 2011;36:957-65.

[29] Danao LA, Edwards J, Eboibi O, Howell R. A numerical investigation into the influence of unsteady wind on the performance and aerodynamics of a vertical axis wind turbine. Appl Energy 2014;116:111-24.

[30] Thakker A, Dhanasekaran TS. Experimental and computational analysis on guide vane losses of impulse turbine for wave energy conversion. Renew Energy 2005;30:1359-72.

[31] Abe K, Nishida M, Sakurai A, Ohya Y, Kihara H, Wada E, et al. Experimental and numerical investigations of flow fields behind a small wind turbine with a flanged diffuser. J Wind Eng Ind Aerodynam 2005;93:951-70.

[32] Lanzafame R, Mauro S, Messina M. Wind turbine CFD modeling using a correlation-based transitional model. Renew Energy 2013;52:31-9.

[33] Thakker A, Hourigan F. Computational fluid dynamics analysis of a 0.6m, 0.6 hub-to-tip ratio impulse turbine with fixed guide vanes. Renew Energy 2005;30:1387-99.

[34] Kishore RA, Priya S. Design and experimental verification of a high efficiency small wind energy portable turbine (SWEPT). J Wind Eng Ind Aerodynam 2013;118:12-9.

[35] Duquette MM, Visser KD. Numerical implications of solidity and blade number on rotor performance of horizontal-axis wind turbines. J Solar Energy Eng 2003;125:425-32.

[36] Ying P. Investigation of a novel wind turbine for an omni-flow wind energy system, PhD thesis, University of Hertfordshire, UK; 2014.

[37] Zhang X. Analysis and optimisation of a novel wind turbine turbine, PhD thesis, University of Hertfordshire, UK; 2013.

[38] Rolland S, Newton W, Williams AJ, Croft TN, Gethin DT, Cross M. Simulations technique for the design of a vertical axis wind turbine device with experimental validation. Appl Energy 2013;111:1195-203.